Applied Catalysis B: Environmental 245 (2019) 522–527

Contents lists available at ScienceDirect

Applied Catalysis B: Environmental

journal homepage: www.elsevier.com/locate/apcatb

Perovskite photocatalyst $CsPbBr_{3-x}I_x$ with a bandgap funnel structure for H_2 evolution under visible light

Zihan Guan[a], Yaqiang Wu[a], Peng Wang[a,*], Qianqian Zhang[a], Zeyan Wang[a], Zhaoke Zheng[a], Yuanyuan Liu[a], Ying Dai[b], Myung-Hwan Whangbo[c], Baibiao Huang[a,*]

[a] State Key Laboratory of Crystal Materials, Shandong University, Jinan 250100, China
[b] School of Physics, Shandong University, Jinan 250100, China
[c] Department of Chemistry, North Carolina State University, Raleigh, NC 27695-8204, United States

ARTICLE INFO

Keywords:
All-inorganic perovskite
Photocatalysis
Halide gradient
Bandgap funnel
Hydrogen evolution

ABSTRACT

A simple and efficient light-assisted method is employed to prepare powder samples of all-inorganic mixed-perovskite $CsPbBr_{3-x}I_x$ from $CsPbBr_3$ by ion exchange in aqueous HBr/KI solution such that the concentration of I in a sample particle decreases on going from the surface to the interior. $CsPbBr_{3-x}I_x$/Pt, namely, $CsPbBr_{3-x}I_x$ samples loaded with Pt nanoparticles, shows a high performance for the hydrogen evolution under visible-light irradiation in aqueous HBr solution saturated with $CsPbBr_3$. The H_2 evolution rate of the $CsPbBr_{3-x}I_x$/Pt powders (200 mg) is determined to be 224 μmol h^{-1}, under 120 mW cm^{-2} visible-light ($\lambda \geq 420$ nm) illumination. The $CsPbBr_{3-x}I_x$ samples have a high stability, with no apparent decrease in the catalytic activity after 50 h of repeated H_2 evolution experiments. The apparent quantum efficiency of $CsPbBr_{3-x}I_x$/Pt is determined to be 2.15% under the irradiation of 450 nm light.

1. Introduction

Organic-inorganic halide perovskite materials possess a high extinction coefficient, a wide absorption range and a long electron-hole diffusion length, so they have triggered great interest for their optoelectronic applications in photovoltaic devices. Remarkable photoelectric conversion efficiencies (from 3.8%–22.1%) have been achieved for perovskite solar cells (PSCs) within just a few years [1–7]. However, the stability of the perovskite material presents a major technical hurdle to commercialization. Compared to the $MAPbI_3$ (MA = CH_3NH_3), all-inorganic perovskite materials $CsPbX_3$ (X = Cl, Br, I) show better stabilities, and have been widely used in photovoltaic devices, light emitting diodes (LEDs), lasers and displays [8–13]. To integrate high stability with quantum confinement effects, Kovalenko et al. fabricated the cesium lead halides ($CsPbX_3$, X = Cl, Br, I) quantum dots (QDs) to find that they have outstanding optical properties, especially their tunable and high-quantum-yield photoluminescence (PL) [14]. In addition, Song et al. synthesized high-quality $CsPbX_3$ QDs through a hot injection method and developed the QD-based quantum light emitting diods (QLEDs) with sharp emissions [15]. Furthermore, Swarnkar et al. reported the formation of α-$CsPbI_3$ QD films that were phase-stable for months in ambient air. These films were used to fabricate colloidal perovskite QD photovoltaic cells with an open-circuit voltage of 1.23 V and efficiency of 10.77% [16].

Compared with $CsPbX_3$ (X = Cl, Br, I), the mixed halide $CsPbBr_{3-x}I_x$ ($0 \leq x \leq 1$) provides a way to improve perovskite solar cells by expanding the bandgap and increasing the stability [17–20]. $CsPbBr_{3-x}I_x$ films, prepared by soaking $CsPbBr_3$ in the 1-octadecene solution of PbI_2 at 170 °C, shows that the concentration of I is highest on the film surface and decreases gradually on going to the interior of the film, and this I-concentration gradient aids the separation of photogenerated electron-hole pairs in $CsPbBr_{3-x}I_x$ mixed halide solar [21]. In addition, Li et al. fabricated perovskite solar cells based on the $MAPbI_3$-$CsPbBr_xI_{3-x}$ heterojunction, to achieve a significantly enhanced PCE of 11.33%. This heterojunction demonstrated an enhancement of hole extraction and conduction from the light absorption layer to the counter electrode [22]. Furthermore, $CsPbX_3$ (X = Cl, Br, I) nanocrystals of different compositions can be readily prepared, and the photoluminescence of $CsPbX_3$ can be tuned over the entire visible spectral region and maintained high quantum yields of 20–80% by adjusting the halide ratios in the colloidal nanocrystal solution [23].

Recently, Nam et al. reported that $MAPbI_3$ powder drives the photocatalytic splitting of HI for hydrogen (H_2) evolution and is stable in a series of saturated aqueous solutions of $MAPbI_3$ by precisely controlling

* Corresponding authors.
E-mail addresses: pengwangicm@sdu.edu.cn (P. Wang), bbhuang@sdu.edu.cn (B. Huang).

https://doi.org/10.1016/j.apcatb.2019.01.019
Received 31 October 2018; Received in revised form 1 January 2019; Accepted 8 January 2019
Available online 08 January 2019
0926-3373/

the ion concentrations (H^+ and I^-) [24]. The $MAPbI_3$/rGO composite, where rGO refers to reduced graphene oxide, prepared by using a facile and efficient photoreaction method at room temperature, was found to be an outstanding photocatalyst for HI splitting [25]. Very recently, our research team found that $MAPbBr_{3-x}I_x$ exhibits an excellent hydrogen production performance in mixed HBr/HI solution saturated with $MAPbBr_3$ [26]. The $MAPbBr_{3-x}I_x$ particle has a bandgap funnel structure, namely, its bandgap becomes larger on going from the surface to the interior. This bandgap funnel structure enhances the transfer of photogenerated charge carriers from the interior to the surface, resulting in the superb photocatalytic performance. As for the photocatalytic use of $CsPbX_3$, there was a report on the photocatalytic CO_2 reduction using a composite of $CsPbBr_3$ perovskite QDs with graphene oxide in ethyl acetate [27,28]. However, this photocatalyst, though stable in ethyl acetate, is not stable in aqueous solution. So far, there has been no report on the preparation and photocatalytic applications in aqueous solution for either $CsPbX_3$ (X = Cl, Br, I) or $CsPbBr_{3-x}I_x$. These results prompted us to construct a crystallization and dissolution equilibrium system to realize the stable existence of $CsPbX_3$ perovskite, and further promote its photocatalytic use for H_2 evolution, in its saturated aqueous haloid acid solution. In the present work, we prepare powder samples of $CsPbBr_{3-x}I_x$ that have a bandgap-funnel structure and show that $CsPbBr_{3-x}I_x$ is more stable than $MAPbBr_{3-x}I_x$, and that $CsPbBr_{3-x}I_x$/Pt also has a high photocatalytic activity for H_2 evolution, which is higher than $MAPbI_3$/rGO but lower than $MAPbBr_{3-x}I_x$/Pt. The band diagram transformation from $CsPbBr_3$ to $CsPbI_3$ shows a funnel structure as shown in Fig. 1. The bandgap funnel structure promotes the transfer of photo-generated electrons and holes from the internal to the surface of the sample, leading to the excellent photocatalytic performance.

2. Experimental

2.1. Chemicals

Lead bromide ($PbBr_2$, 99%, Aladdin); Caesium bromide (CsBr, 99.9%, Aladdin); Hydrobromic acid (HBr, 48 wt. % in H_2O, 99.99% metals basis, Aladdin); Potassium iodide (KI, 99%, Aladdin); Chloroplatinic acid ($H_2PtCl_6{\cdot}6H_2O$, 97%). All the chemicals are analytical reagents without further purification.

2.2. Preparation of $CsPbBr_3$

$CsPbBr_3$ powders were fabricated using a simple solid state sintering method [29]. A mixture of 367 mg $PbBr_2$ and 213 mg CsBr evenly (molar ratio of 1:1) was grind for about 30 min to get homogeneous

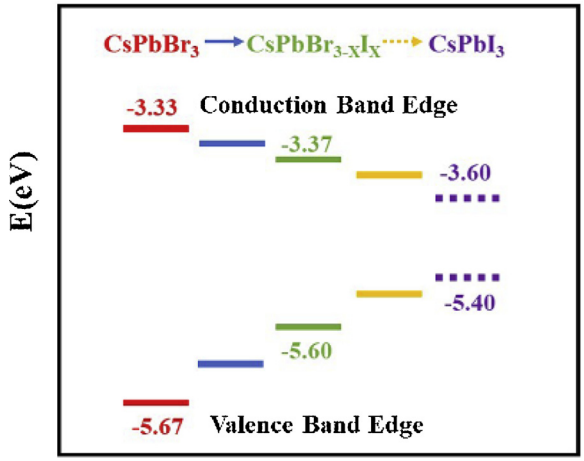

Fig. 1. Band diagram of the $CsPbBr_3$, $CsPbBr_{3-x}I_x$ and $CsPbI_3$.

powers, which were transferred to a furnace and were heated up to 400 °C at the rate of 10 °C/min. The powders were kept at 400 °C for 2 h and then naturally cooled to room temperature. The products were further ground to obtain powder samples of $CsPbBr_3$.

2.3. Preparation of $CsPbBr_{3-x}I_x$

Excess of $CsPbBr_3$ powders were added into HBr acid solution and stirred for 2 h to obtain the saturated solution. 400 mg KI and 200 mg $CsPbBr_3$ were dispersed in 50 ml aqueous HBr acid solution saturated with $CsPbBr_3$, and then the solution was exposed to visible light ($\lambda \geq 420$ nm) and kept stirring for different durations of time (10 s, 1 min, 5 min, 10 min, 30 min, 1 h, 2 h). The as-prepared $CsPbBr_{3-x}I_x$ samples were centrifuged, dried and preserved for further reactions and characterizations.

2.4. Preparation of Pt-loaded $CsPbBr_{3-x}I_x$

$CsPbBr_{3-x}I_x$/Pt was obtained using a photoreduction method [25]. 150 μL chloroplatinic acid (0.0772 mol/L $H_2PtCl_6{\cdot}6H_2O$ dissolved in deionized water) was added into the mentioned saturated solution with stirring, then the mixture was treated by ultrasonic for 10 min, which was followed by another 20 min of stirring to get the mixture homogeneous. The suspension was then exposed to visible light irradiation produced by Xe lamp with a 420 nm cut-off filter for 1 h allowing for the photoreduction. The whole process was kept at 15 °C using a water-cooling system. The saturated solution with 200 mg $CsPbBr_{3-x}I_x$/Pt was used for the H_2 evolution measurements. The chemicals used as well as the characterization and measurements are described in the Supporting Information (SI).

3. Results and discussion

3.1. Characterization of $CsPbBr_{3-x}I_x$

The X-ray diffraction (XRD) profiles of the products fabricated at different reaction time (Fig. 2a) show that, as the exchange reaction proceeds, the diffraction peaks shift steadily to a lower 2θ value. This reveals that the lattice constants of $CsPbBr_{3-x}I_x$ increases with increasing the reaction time, which reflects that more Br^- are replaced by larger I- ions with increasing the reaction time. The samples obtained under 1 h of light irradiation show a peak shift of 0.15°, and this position hardly changes invariable after 1 h. No additional diffraction peaks appear in the spectra, confirming that the $CsPbBr_3$ crystal structure remains cubic throughout the exchange. Scanning electron microscope (SEM) images of $CsPbBr_3$ and $CsPbBr_{3-x}I_x$ are presented in **Figure S1**, which shows that the $CsPbBr_{3-x}I_x$ particles have smoother surfaces. The SEM image of $CsPbBr_{3-x}I_x$ in Fig. 2**b** shows that wafers of 2μm in average size are precipitated from the solution on the surface. The energy dispersive spectroscopy (EDS) mapping of the elements of $CsPbBr_{3-x}I_x$ carried out for the sample area shown in Fig. 2**c** are presented in Fig. 2d–g). The elements Cs, Pb, Br and I are uniformly distributed on the particles, proving that the exchange between Br^- and I^- has taken place homogenously throughout the surface of the sample surface. As summarized in **Table S1**, the Br to I atom ratio in $CsPbBr_{3-x}I_x$ sample is 96:1 for the light irradiation of 10 s, and 29:1 for the light irradiation of 1 h. As shown in **Figure S2**, the color of the $CsPbBr_{3-x}I_x$ sample becomes gradually darker with increasing the reaction time. This is so because the concentration of I in $CsPbBr_{3-x}I_x$ increases with increasing the reaction time.

To verify the substitution of I^- for Br^-, we carry out X-ray photoelectron spectroscopy (XPS) measurements for $CsPbBr_3$ and $CsPbBr_{3-x}I_x$ (sample obtained for 1 h of the reaction). The Pb $4f_{7/2}$ and Pb $4f_{5/2}$ peaks of $CsPbBr_3$ are located at 138.0 and 142.9 eV, respectively (Fig. 3a), and the Br $3d_{5/2}$ and Br $3d_{3/2}$ peaks of $CsPbBr_3$ at 68.0 and 69.0 eV, respectively (Fig. 3b). In $CsPbBr_{3-x}I_x$, the Pb 4f peaks are

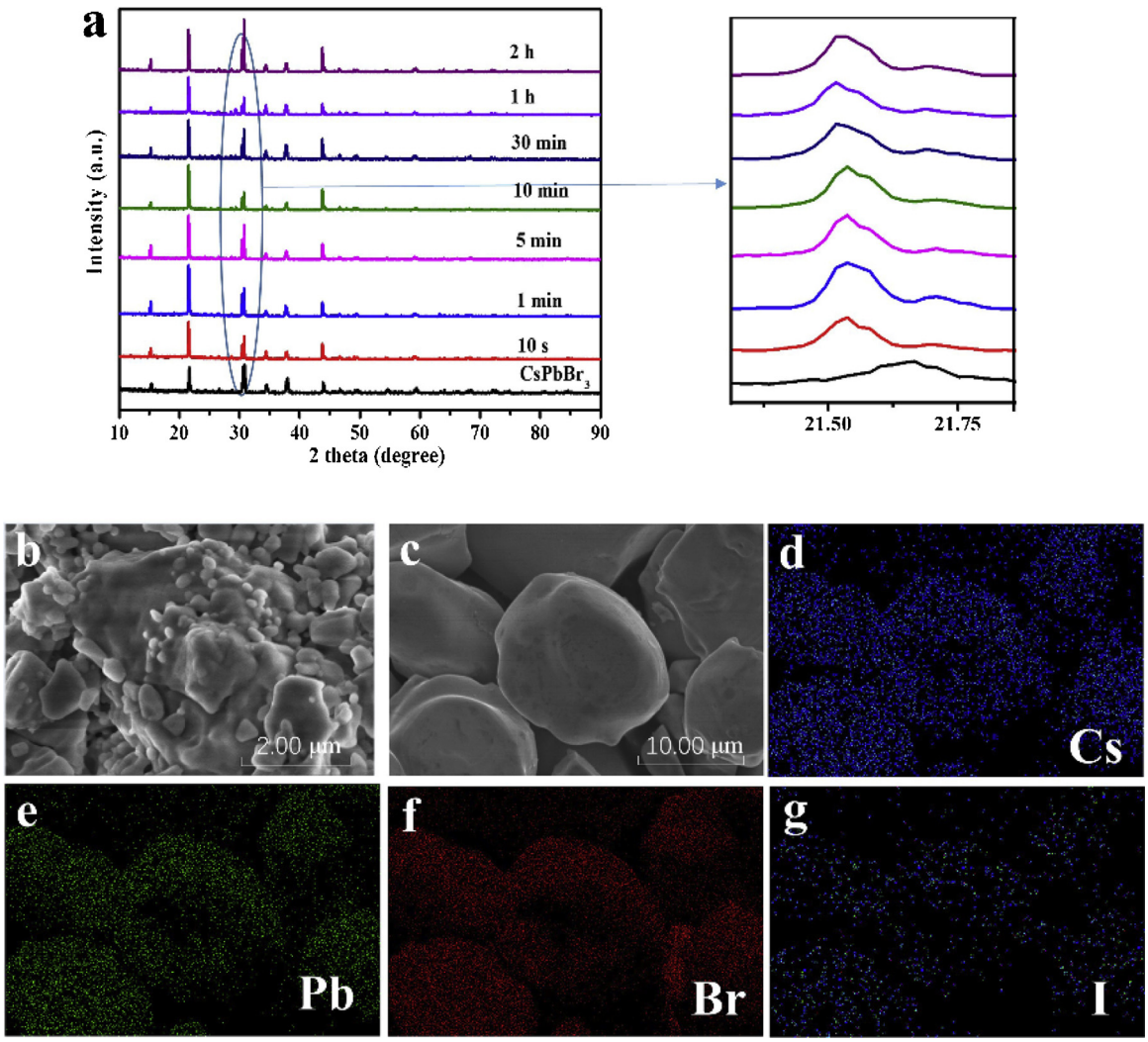

Fig. 2. (a) XRD patterns of the $CsPbBr_{3-x}I_x$ particles obtained at different exchange time. (b, c) SEM images of $CsPbBr_{3-x}I_x$ particles. (d – g) EDS mapping images of the Cs, Pb, Br, and I elements of $CsPbBr_{3-x}I_x$ for the area shown in Fig. 2**c**.

shifted toward a higher binding energy (~0.35 eV), but the Br 3d peaks are hardly shifted. In addition, each of the two Pb 4f peaks is split into two subpeaks in $CsPbBr_{3-x}I_x$, which provides a convincing proof for the substitution of I^- for Br^-. In each subpeak, the higher binding energy peak is assigned to the Pb-Br bonds and the lower one to Pb-I bonds. To determine whether there is K^+ and Pt particles in the $CsPbBr_{3-x}I_x$/Pt, XPS spectra of K 2p and Pt 4f are shown in **Figure S3**.

3.2. Bandgap funnel structure

To investigate the influence of the halide ion exchange on the bandgap of $CsPbBr_{3-x}I_x$, we carried out transient absorption measurements. Fig. 4**a** compares the transient absorption spectra of the perovskites before and after the 1 h of the halide ion exchange. The absorption spectrum of $CsPbBr_3$ displays a strong bleach at 516 nm

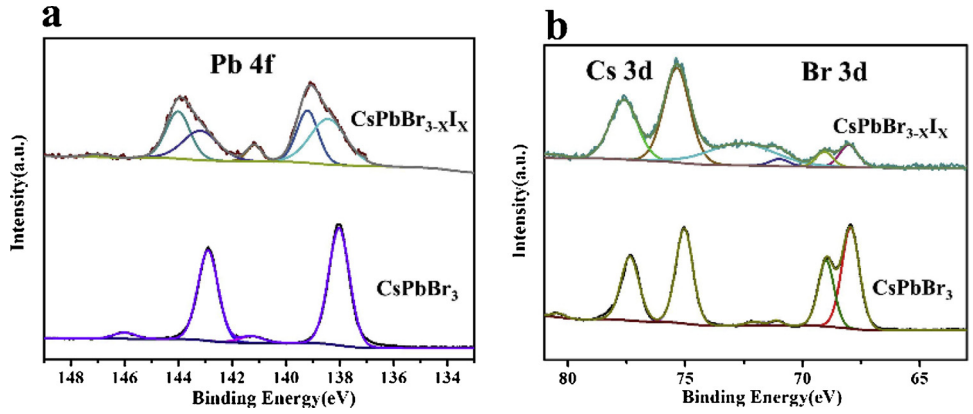

Fig. 3. High-resolution XPS spectra of $CsPbBr_3$ (below) and $CsPbBr_{3-x}I_x$ (upper) for (a) Pb 4f and (b) Br 3d states.

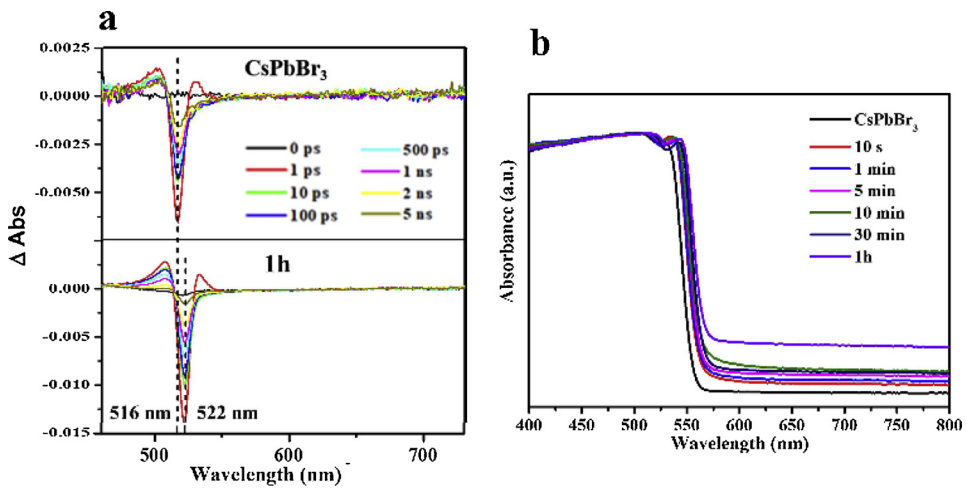

Fig. 4. (a) Transient absorption spectra of $CsPbBr_3$ before and after the 1 h of the ion-exchange reaction; (b) The UV–vis diffuse reflectance spectra of $CsPbBr_{3-x}I_x$ powders taken at different halide exchange reaction times.

corresponding to the bandgap of $CsPbBr_3$. After 1 h of the halide ion exchange, the main bleach is red-shifted by about 6 nm, in agreement with the previous report. [21] A signal for the transient absorption spectra of $CsPbI_3$ is not observed, revealing that the I^- ions of $CsPbBr_{3-x}I_x$ substituted for the Br^- ions only exist within a limited thickness of the perovskite particle surface. Fig. 4**b** shows the UV–vis diffuse spectra of $CsPbBr_{3-x}I_x$. The absorption onset of $CsPbBr_3$ is located at 556 nm (a bandgap of 2.3 eV), which matches well with the previous report. [30] With increasing the time of the halide ion exchange reaction, the concentration of iodine ions in $CsPbBr_{3-x}I_x$ rises up gradually and the absorption onset red-shifts to around 570 nm. Furthermore, the absorption tails covering from ~565 nm across the entire red-light region, become stronger with increasing the reaction time. The action spectra (wavelength dependent) of H_2 production reaction of $CsPbBr_{3-x}I_x$/Pt under various monochromatic light irradiations (left axis) has been shown in **Figure S4**. As can be seen, the variation tendency of H_2 production is similar to the UV/Vis light absorption spectrum (right axis).These results indicate an increasing amount of I- substitution and a broader I- distribution in $CsPbBr_{3-x}I_x$, which are consistent with our previous report. [26] Since the anion-exchange reaction begins from the surface of $CsPbBr_{3-x}I_x$ particles, it is reasonable that the concentration of I- in $CsPbBr_{3-x}I_x$ is largest in the surface and gets less on moving to the interior. Thus, the corresponding bandgap of $CsPbBr_{3-x}I_x$ would be narrowest in the surface iodide-rich region and become wider on going to the interior bromide-rich region [31], constructing a bandgap funnel structure.

To verify that the as-prepared $CsPbBr_{3-x}I_x$ has the bandgap funnel structure, we carry out photoluminescence (PL) and the ground-state-bleach (GSB) signal measurements. Fig. 5**a** shows the PL spectra of the as-prepared $CsPbBr_{3-x}I_x$ determined at various reaction times (from 10 s to 2 h). With increasing the halide-ion-exchange reaction time, the intensity of the characteristic PL peaks around 523 nm decreases continuously while that of a broad peak emerging around 662 nm increases continuously. The PL peaks at 662 nm are assigned to the electron-hole recombination in the I-rich region of $CsPbBr_{3-x}I_x$. These results are consistent with the presence of a bandgap funnel structure in $CsPbBr_{3-x}I_x$, as discussed in the case of $MAPbBr_{3-x}I_x$ [26]. The PL peaks are rather broad because the I element has a relatively broad distribution in the region near the particle. The GSB signal of $CsPbBr_{3-x}I_x$ shows a faster recovery kinetics with longer reaction time (Fig. 5b), indicating the carrier transport from the internal Br-rich region to the surface I-rich region. Since a longer halide-exchange reaction time leads to a larger surface I-rich domain, a faster carrier transport kinetics occurs.

To examine the bandgap funnel structure more directly, etched a powder particle of the $CsPbBr_{3-x}I_x$ sample (obtained for 1 h of halide-ion exchange time) were etched with argon ions for 0, 30, 60 and 100 s to probe the elements at four different levels of depths from the surface by XPS measurements. The valence band maximum (VBM) measured on the sample surface is 1.13 eV, which shifts gradually toward higher binding energy at 1.53 eV after etched for 100 s (Fig. 6a). Gradient change of the valence band constitute this grade heterojunction, which promote the transfer of photo-generated electrons and holes from the internal to the surface of the sample. By measuring and calculating the peak area of I^- and Br^-, we determine their relative intensities as a function of the etching time (Fig. 6b). With increasing the etching time (and hence the depth from the surface), the bromine to iodine ratio increases gradually. This shows that the concentration of I in a $CsPbBr_{3-x}I_x$ particle decreases gradually on going from the surface to the

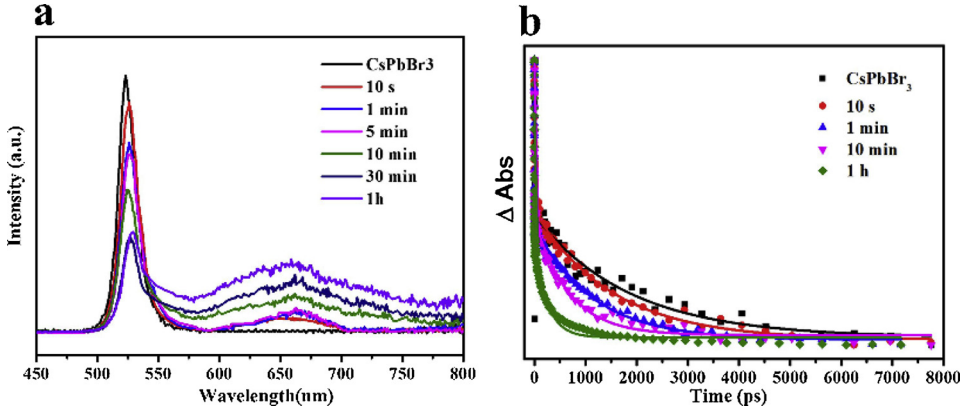

Fig. 5. (a) Photoluminescence (PL) spectrum of $CsPbBr_{3-x}I_x$ powders taken at different halide exchange times; (b) Comparison of the ground state bleach recovery kinetics of $CsPbBr_3$ after 0, 10 s, 1 m, 10 m and 1 h of the ion-exchange reaction. The solid lines are the fits of the kinetics to a bi-exponential function with the average lifetimes τ.

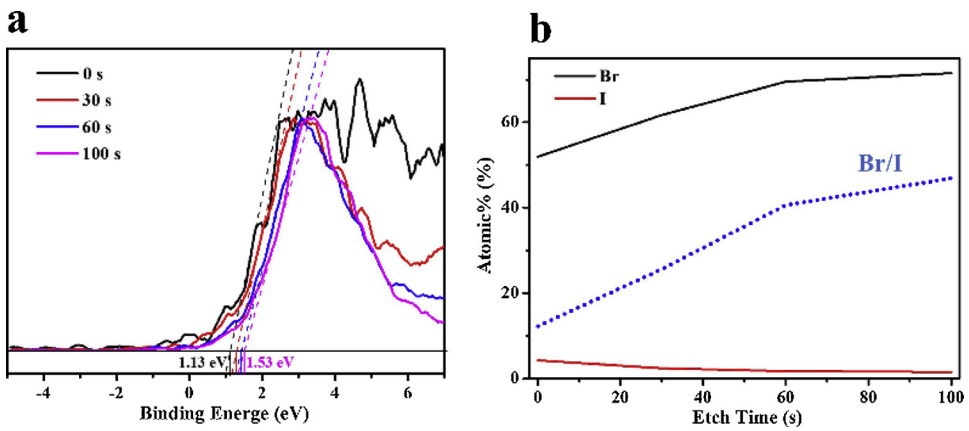

Fig. 6. (a) XPS depth profiling for the valence band of $CsPbBr_{3-x}I_x$ particles at four different etching time (i.e., 0, 30, 60, and 100 s); (b) Atomic content of Br and I in $CsPbBr_{3-x}I_x$ powders at different etching time.

interior.

3.3. Photocatalytic activity

We now evaluate the photocatalytic performance of $CsPbBr_{3-x}I_x$ for H_2 evolution. $CsPbBr_3$ samples are not efficient for H_2 evolution (Fig. 7a), nor are the $CsPbBr_3$ samples loaded with Pt as a cocatalyst. However, in saturated HBr solution of $CsPbBr_3$, $CsPbBr_{3-x}I_x$ is highly efficient for H_2 evolution when exposed to the visible light ($\lambda \geq 420$ nm), with the rate of 23.6 μmol h^{-1} (200 mg photocatalyst). To reduce the over-potential in the production of H_2 from water and suppress the fast backward reaction, we loaded $CsPbBr_{3-x}I_x$ samples with Pt as a cocatalyst. The doping levels of I- and Pt have been optimized as shown in **Figure S5**. Under the same measuring conditions, the reactivity of the $CsPbBr_{3-x}I_x$/Pt samples is found much greater than that of $CsPbBr_{3-x}I_x$ (224 vs. 23.6 μmol h^{-1}) which is much better than the previously reported performance of $MAPbI_3$/rGO (93.9 μmol h^{-1}). [25] The apparent quantum efficiency of $CsPbBr_{3-x}I_x$/Pt was determined to be 2.15% under the irradiation of 450 nm light (**Figure S6**). Moreover, $CsPbBr_{3-x}I_x$/Pt has an excellent stability, which shows no significant decline in the activity for the H_2 evolution after 5 cycles of 10 h repeated experiments (Fig. 7b). This good stability could be attributed in part to the dynamic equilibrium between the powder samples surface and saturated solution during the photocatalytic reaction process.

It should be noted that I^- exists in the reaction solution and would act as a sacrificial reagent to consume photogenerated holes, producing the I_3- species during the reaction process. However, the I_3- species darken the solution and obstruct the light absorption of the catalyst. Thus, we added H_3PO_2 to effectively and selectively reduce I_3-, which results in the misbalance between the amount of H_2 and I_3-. Control experiments indicated that no appreciable hydrogen was produced in the absence of irradiation, and little hydrogen production was detected in the absence of photocatalyst (**Figure S7**), suggesting that hydrogen was produced by photocatalytic reactions of $CsPbBr_{3-x}I_x$. The $CsPbBr_{3-x}I_x$ without compositional gradient lost hydrogen evolution reactivities in 3 h (**Figure S8**), proving effect of the bandgap funnel structure.

4. Conclusions

In summary, we prepared an all-inorganic perovskite $CsPbBr_{3-x}I_x$ with bandgap funnel structure, using a facile and efficient photoreaction method at room temperature in aqueous solution. The $CsPbBr_{3-x}I_x$/Pt samples have a superb H_2 evolution activity and are very stable in $CsPbBr_3$-saturated aqueous HBr solution. This excellent photocatalytic performance primarily because $CsPbBr_{3-x}I_x$ has a bandgap funnel structure, which promotes the transfer of photo-generated electrons and holes from the internal to the surface of the sample. Our study on $CsPbBr_{3-x}I_x$ and previous study on $MAPbBr_{3-x}I_x$ provide an approach to stabilize perovskites materials in aqueous solution and extend their applications in photocatalysis.

Acknowledgements

This work was financially supported by the National Natural Science Foundation of China (51602179, 21333006, 21573135, and 11374190), and the National Basic Research Program of China (973 program, 2013CB632401), P.W. acknowledges support from the Taishan Scholars Program of Shandong Province.

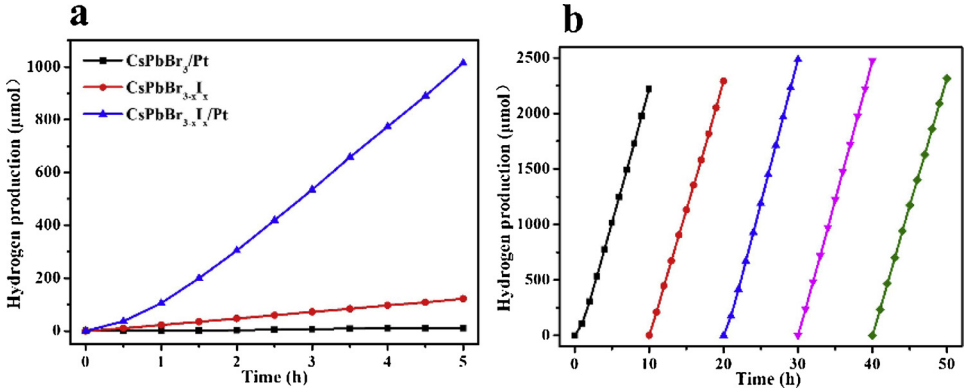

Fig. 7. (a) Comparison of the H_2 evolution activities of $CsPbBr_3$, $CsPbBr_{3-x}I_x$ and $CsPbBr_{3-x}I_x$/Pt; (b) H_2 evolution activity of $CsPbBr_{3-x}I_x$/Pt during the first five cycles of repeated experiments.

Appendix A. Supplementary data

Supplementary material related to this article can be found, in the online version, at doi:https://doi.org/10.1016/j.apcatb.2019.01.019.

References

[1] J. Qiu, Y. Qiu, K. Yan, M. Zhong, C. Mu, H. Yan, S. Yang, All-solid-state hybrid solar cells based on a new organometal halide perovskite sensitizer and one-dimensional TiO_2 nanowire arrays, Nanoscale 5 (2013) 3245–3248.

[2] W. Rehman, R.L. Milot, G.E. Eperon, C. Wehrenfennig, J.L. Boland, H.J. Snaith, M.B. Johnston, L.M. Herz, Charge-carrier dynamics and Mobilities in formamidinium lead mixed-halide perovskites, Adv. Mater. 27 (2015) 7938–7944.

[3] L.C. Schmidt, A. Pertegas, S. Gonzalez-Carrero, O. Malinkiewicz, S. Agouram, G. Minguez Espallargas, H.J. Bolink, R.E. Galian, J. Perez-Prieto, Nontemplate synthesis of $CH_3NH_3PbBr_3$ perovskite nanoparticles, J. Am. Chem. Soc. 136 (2014) 850–853.

[4] W.-L. Xu, M.-S. Niu, X.-Y. Yang, H.-C. Yuan, C. Xiong, X.-F. Zhu, X.-T. Hao, Aqueous self-assembled perovskite microfibers for sensitive photodetectors, Org. Electron. 48 (2017) 106–111.

[5] M. Wei, M. Niu, P. Bi, X. Hao, S. Ren, S. Xie, W. Qin, Optically controlled magnetization and magnetoelectric effect in organic multiferroic heterojunction, Adv. Opt. Mater. 5 (2017) 1700644.

[6] Y. An, Y. Liu, P. An, J. Dong, B. Xu, Y. Dai, X. Qin, X. Zhang, M.-H. Whangbo, B. Huang, Ni^{II} coordination to an Al-based metal-organic framework made from 2-aminoterephthalate for photocatalytic overall water splitting, Angew. Chem. Int. Ed. 129 (2017) 3082–3086.

[7] X. Liu, P. Wang, H. Zhai, Q. Zhang, B. Huang, Z. Wang, Y. Liu, Y. Dai, X. Qin, X. Zhang, Synthesis of synergetic phosphorus and cyano groups ($-C\equiv N$) modified g–C3N4 for enhanced photocatalytic H2 production and CO_2 reduction under visible light irradiation, Appl. 232 (2018) 521–530.

[8] R. Begum, M.R. Parida, A.L. Abdelhady, B. Murali, N.M. Alyami, G.H. Ahmed, M.N. Hedhili, O.M. Bakr, O.F. Mohammed, Engineering interfacial charge transfer in $CsPbBr_3$ perovskite nanocrystals by heterovalent doping, J. Am. Chem. Soc. 139 (2017) 731–737.

[9] G. Li, H. Wang, Z. Zhu, Y. Chang, T. Zhang, Z. Song, Y. Jiang, Shape and phase evolution from $CsPbBr_3$ perovskite nanocubes to tetragonal $CsPb_2Br_5$ nanosheets with an indirect bandgap, Chem. Commun. 52 (2016) 11296–11299.

[10] D. Zhang, Y. Yang, Y. Bekenstein, Y. Yu, N.A. Gibson, A.B. Wong, S.W. Eaton, N. Kornienko, Q. Kong, M. Lai, A.P. Alivisatos, S.R. Leone, P. Yang, Synthesis of composition tunable and highly luminescent cesium lead halide nanowires through anion-exchange reactions, J. Am. Chem. Soc. 138 (2016) 7236–7239.

[11] J. Ding, S. Du, Z. Zuo, Y. Zhao, H. Cui, X. Zhan, High detectivity and rapid response in perovskite CsPbBr3 single-crystal photodetector, J. Phys. Chem. C 121 (2017) 4917–4923.

[12] B. Wang, J. Di, P. Zhang, J. Xia, S. Dai, H. Li, Ionic liquid-induced strategy for porous perovskite-like $PbBiO_2Br$ photocatalysts with enhanced photocatalytic activity and mechanism insight, Appl. Catal. B 206 (2017) 127–135.

[13] X. Zhu, P. Wang, B. Huang, X. Ma, X. Qin, X. Zhang, Y. Dai, Synthesis of novel visible light response $Ag_{10}Si_4O_{13}$ photocatalyst, Appl. Catal. B 199 (2016) 315–322.

[14] L. Protesescu, S. Yakunin, M.I. Bodnarchuk, F. Krieg, R. Caputo, C.H. Hendon, R.X. Yang, A. Walsh, M.V. Kovalenko, Nanocrystals of cesium lead halide perovskites (CsPbX(3), X = Cl, Br, and I): novel optoelectronic materials showing bright emission with wide color gamut, Nano Lett. 15 (2015) 3692–3696.

[15] J. Song, J. Li, X. Li, L. Xu, Y. Dong, H. Zeng, Quantum dot light-emitting diodes based on inorganic perovskite cesium lead halides ($CsPbX_3$), Adv Mater. 27 (2015) 7162–7167.

[16] A. Swarnkar, A.R. Marshall, E.M. Sanehira, B.D. Chernomordik, D.T. Moore, J.A. Christians, T. Chakrabarti, J.M. Luther, Quantum dot-induced phase stabilization of alpha-$CsPbI_3$ perovskite for high-efficiency photovoltaics, Science 354 (2016) 92–95.

[17] V. Gonzalez-Pedro, E.J. Juarez-Perez, W.S. Arsyad, E.M. Barea, F. Fabregat-Santiago, I. Mora-Sero, J. Bisquert, General working principles of $CH_3NH_3PbX_3$ perovskite solar cells, Nano Lett. 14 (2014) 888–893.

[18] D.-H. Kwak, D.-H. Lim, H.-S. Ra, P. Ramasamy, J.-S. Lee, High performance hybrid graphene–$CsPbBr_{3-x}I_x$ perovskite nanocrystal photodetector, RSC Adv. 6 (2016) 65252–65256.

[19] X. Liang, P. Wang, M. Li, Q. Zhang, Z. Wang, Y. Dai, X. Zhang, Y. Liu, M.-H. Whangbo, B. Huang, Adsorption of gaseous ethylene via induced polarization on plasmonic photocatalyst $Ag/AgCl/TiO_2$ and subsequent photodegradation, Appl. Catal. B 220 (2018) 356–361.

[20] H. Bian, D. Bai, Z. Jin, K. Wang, L. Liang, H. Wang, J. Zhang, Q. Wang, S. Liu, Graded bandgap $CsPbI_{2+x}Br_{1-x}$ perovskite solar cells with a stabilized efficiency of 14.4%, Joule 2 (2018) 1500–1510.

[21] J.B. Hoffman, A.L. Schleper, P.V. Kamat, Transformation of sintered $CsPbBr_3$ nanocrystals to cubic $CsPbI_3$ and gradient $CsPbBr_xI_{3-x}$ through halide exchange, J. Am. Chem. Soc. 138 (2016) 8603–8611.

[22] B. Li, Y. Zhang, L. Zhang, L. Yin, Graded heterojunction engineering for hole-conductor-free perovskite solar cells with high hole extraction efficiency and conductivity, Adv Mater. 29 (2017).

[23] G. Nedelcu, L. Protesescu, S. Yakunin, M.I. Bodnarchuk, M.J. Grotevent, M.V. Kovalenko, Fast anion-exchange in highly luminescent nanocrystals of cesium lead halide perovskites ($CsPbX_3$, X = Cl, Br, I), Nano Lett. 15 (2015) 5635–5640.

[24] S. Park, W.J. Chang, C.W. Lee, S. Park, H.-Y. Ahn, K.T. Nam, Photocatalytic hydrogen generation from hydriodic acid using methylammonium lead iodide in dynamic equilibrium with aqueous solution, Nat. Energy 2 (2016) 16185.

[25] Y. Wu, P. Wang, X. Zhu, Q. Zhang, Z. Wang, Y. Liu, G. Zou, Y. Dai, M.H. Whangbo, B. Huang, Composite of $CH_3NH_3PbI_3$ with reduced graphene oxide as a highly efficient and stable visible-light photocatalyst for hydrogen evolution in aqueous HI solution, Adv Mater. 30 (2018) 1704342.

[26] Y. Wu, P. Wang, Z. Guan, J. Liu, Z. Wang, Z. Zheng, S. Jin, Y. Dai, M.-H. Whangbo, B. Huang, Enhancing the photocatalytic hydrogen evolution activity of mixed-halide perovskite $CH_3NH_3PbBr_{3-x}I_x$ achieved by Bandgap Funneling of charge carriers, ACS Catal. 8 (2018) 10349–10357.

[27] Y.F. Xu, M.Z. Yang, B.X. Chen, X.D. Wang, H.Y. Chen, D.B. Kuang, C.Y. Su, A $CsPbBr_3$ perovskite quantum Dot/Graphene oxide composite for photocatalytic CO_2 reduction, J. Am. Chem. Soc. 139 (2017) 5660–5663.

[28] X. Lin, Y. Gao, M. Jiang, Y. Zhang, Y. Hou, W. Dai, S. Wang, Z. Ding, Photocatalytic CO_2 reduction promoted by uniform perovskite hydroxide $CoSn(OH)_6$ nanocubes, Appl. Catal. B 224 (2018) 1009–1016.

[29] C.C. Stoumpos, C.D. Malliakas, J.A. Peters, Z. Liu, M. Sebastian, J. Im, T.C. Chasapis, A.C. Wibowo, D.Y. Chung, A.J. Freeman, B.W. Wessels, M.G. Kanatzidis, Crystal growth of the perovskite semiconductor $CsPbBr_3$: a new material for high-energy radiation detection, Cryst. Growth Des. 13 (2013) 2722–2727.

[30] J. Liang, P. Zhao, C. Wang, Y. Wang, Y. Hu, G. Zhu, L. Ma, J. Liu, Z. Jin, $CsPb_{0.9}Sn_{0.1}IBr_2$ based all-inorganic perovskite solar cells with exceptional efficiency and stability, J. Am. Chem. Soc. 139 (2017) 14009–14012.

[31] V.K. Ravi, G.B. Markad, A. Nag, Band edge energies and excitonic transition probabilities of colloidal $CsPbX_3$ (X = Cl, Br, I) perovskite nanocrystals, ACS Energy Lett. 1 (2016) 665–671.